Monthly Notices of the ROYAL ASTRONOMICAL SOCIETY

MNRAS **471,** 463–477 (2017)
Advance Access publication 2017 June 23

doi:10.1093/mnras/stx1588

On the timing properties of SAX J1808.4−3658 during its 2015 outburst

A. Sanna,[1★] T. Di Salvo,[2] L. Burderi,[1] A. Riggio,[1] F. Pintore,[3] A. F. Gambino,[2] R. Iaria,[2] M. Tailo,[1,4] F. Scarano[1] and A. Papitto[4]

[1]*Dipartimento di Fisica, Università degli Studi di Cagliari, SP Monserrato-Sestu km 0.7, I-09042 Monserrato, Italy*
[2]*Dipartimento di Fisica e Chimica, Università degli Studi di Palermo, via Archirafi 36, I-90123 Palermo, Italy*
[3]*INAF – Istituto di Astrofisica Spaziale e Fisica Cosmica – Milano, via E. Bassini 15, I-20133 Milano, Italy*
[4]*INAF – Osservatorio Astronomico di Roma, Via di Frascati 33, I-00044 Monteporzio Catone (Roma), Italy*

Accepted 2017 June 20. Received 2017 June 20; in original form 2017 March 13

ABSTRACT

We present a timing analysis of the 2015 outburst of the accreting millisecond X-ray pulsar SAX J1808.4−3658, using non-simultaneous *XMM–Newton* and *NuSTAR* observations. We estimate the pulsar spin frequency and update the system orbital solution. Combining the average spin frequency from the previous observed, we confirm the long-term spin-down at an average rate $\dot{\nu}_{\rm SD} = 1.5(2) \times 10^{-15}$ Hz s^{-1}. We also discuss possible corrections to the spin-down rate accounting for mass accretion on to the compact object when the system is X-ray active. Finally, combining the updated ephemerides with those of the previous outbursts, we find a long-term orbital evolution compatible with a binary expansion at a mean rate $\dot{P}_{\rm orb} = 3.6(4) \times 10^{-12}$ s s^{-1}, in agreement with previously reported values. This fast evolution is incompatible with an evolution driven by angular momentum losses caused by gravitational radiation under the hypothesis of conservative mass transfer. We discuss the observed orbital expansion in terms of non-conservative mass transfer and gravitational quadrupole coupling mechanism. We find that the latter can explain, under certain conditions, small fluctuations (of the order of few seconds) of the orbital period around a global parabolic trend. At the same time, a non-conservative mass transfer is required to explain the observed fast orbital evolution, which likely reflects ejection of a large fraction of mass from the inner Lagrangian point caused by the irradiation of the donor by the magnetodipole rotator during quiescence (*radio-ejection* model). This strong outflow may power tidal dissipation in the companion star and be responsible of the gravitational quadrupole change oscillations.

Key words: accretion, accretion discs – stars: neutron – pulsars: individual: SAX J1808.4−3658 – X-rays: binaries.

1 INTRODUCTION

SAX J1808.4−3658 is a neutron star (NS) low-mass X-ray binary (LMXB) observed for the first time in 1996 by the *BeppoSAX* satellite (in 't Zand et al. 1998). The discovery of the coherent pulsation at roughly 2.5 ms (Chakrabarty & Morgan 1998; Wijnands & van der Klis 1998) made this source the first observed accreting millisecond X-ray pulsar (AMXP). This class of objects is X-ray transients that generate X-ray coherent pulsation by accreting matter on to the NS polar caps. Matter from the companion star is first transferred via Roche lobe overflow, and then interacts with the NS magnetosphere. AMXPs are characterized by long quiescence periods (years to decades) interrupted by short outburst phases (lasting weeks to months) during which the X-ray emission increases by orders of magnitude. Processes such as thermal-viscous instability in a thin disc might be responsible for the episodic accretion rate variations (see e.g. Meyer & Meyer-Hofmeister 1982; Smak 1982), although the outburst trigger mechanism is still highly debated. AMXPs have been proved to be the evolutionary link between radio millisecond pulsars and accreting NS (see e.g. IGR J18245−2452; Papitto et al. 2013), confirming the so-called recycling scenario (see e.g. Bhattacharya & van den Heuvel 1991).

Since its discovery, SAX J1808.4−3658 was observed in outburst seven times (with average recurrence times of roughly 2.5–3.5 yr), including the most recent one started in 2015 April (Sanna et al. 2015). So far, SAX J1808.4−3658 has been the most observed of its class, making it the best candidate to explore the long-term properties of AMXPs. The source exhibited several thermonuclear X-ray bursts in each of the outbursts, some of which were classified as photospheric radius expansion X-ray bursts (Galloway & Cumming 2006; Galloway et al. 2008), most likely originating in a flash of

★ E-mail: andrea.sanna@dsf.unica.it

pure helium layer created by stable burning hydrogen. Combining the X-ray burst from different outbursts, Galloway & Cumming (2006) placed the source at a distance of 3.5 ± 0.1 kpc.

The secular evolution of the spin frequency, up to the 2011 outburst of the source, is compatible with a constant spin-down derivative of magnitude $\sim -10^{-15}$ Hz s^{-1} (Patruno et al. 2012), likely reflecting a magnetic dipole torque acting during quiescence (see also Hartman et al. 2008, 2009b). These effects constraint the magnetic dipole moment at the value $\mu \sim 10^{26}$ G cm^3, corresponding to a surface magnetic field at the NS poles $B \sim 2 \times 10^8$ G (assuming a NS radius of 10 km; Hartman et al. 2008). Similar estimates have been inferred from spectral fitting, more precisely from the study of the broad iron emission line (Cackett et al. 2009; Papitto et al. 2009), and from the modelling of the accretion disc (Ibragimov & Poutanen 2009). Combining the spin frequency and the source luminosity in quiescence, Di Salvo & Burderi (2003) estimated a surface magnetic field in the range (1–5) $\times 10^8$ G. Moreover, the detection of a spin-down frequency derivative of $\sim -8 \times 10^{-14}$ Hz s^{-1} during the final stages of the 2002 outburst, suggested a NS magnetic field of $\sim 3.5 \times 10^8$ G (Burderi et al. 2006).

From the analysis of the orbital modulation of the persistent pulsation has been determined a binary orbital period of $\sim$2 h (Chakrabarty & Morgan 1998), around a companion star of mass likely in the range 0.04–0.14 $M_\odot$ (Bildsten & Chakrabarty 2001; Deloye et al. 2008; Di Salvo et al. 2008; Burderi et al. 2009). Combining the orbital ephemerides of the outbursts up to the 2005, Di Salvo et al. (2008) and Hartman et al. (2008) observed an expansion of the orbital period at a rate of $\sim 3.5 \times 10^{-12}$ s s^{-1}. This result has been confirmed by Hartman et al. (2009b, from the analysis of the *Rossi X-ray Time Explorer* observations) and Burderi et al. (2009, from the analysis of the single *XMM–Newton* observation) that extended the analysis up to the 2008 outburst. The authors found a consistent orbital period derivative, suggesting that the orbital evolution remained stable over the 10 yr baseline considered. The large orbital expansion rate has been interpreted by Di Salvo et al. (2008) and Burderi et al. (2009) as the result of a highly non-conservative mass transfer where only a few per cent of the transferred matter is accreted on to the NS. Hartman et al. (2008, 2009b) suggested that, in analogy with a sample of observed 'black widow' millisecond radio pulsars (Arzoumanian, Fruchter & Taylor 1994; Doroshenko et al. 2001), the orbital period derivative of SAX J1808.4−3658 could have been the result of short-term interchanges of angular momentum between the companion star and the binary system. The latter hypothesis increased consensus after updating the long-term orbital evolution including the 2011 outburst of the source. Patruno et al. (2012) observed that the expansion of the orbital period of SAX J1808.4−3658 requires both a first and second orbital period derivative with values $\dot{P}_{\rm orb} = 3.5(2) \times 10^{-12}$ and $1.65(35) \times 10^{-20}$ s s^{-2}, respectively. The authors proposed a mass quadrupole variation of the companion as the cause of the orbital period changes (Applegate & Shaham 1994). Patruno et al. (2017), reporting a 30-ks *Chandra* observation of the source during the final stages of its 2015 outburst, highlighted that SAX J1808.4−3658 continues evolving with a large orbital period derivative. The authors explained the secular orbital behaviour of the source suggesting that either the NS ablates the donor causing a highly efficient mass loss or the donor star undergoes quasi-cyclic variations caused by magnetically (or irradiation) driven mass-quadrupole changes.

In this work, we carried out a coherent timing analysis of the 2015 outburst of SAX J1808.4−3658, using non-simultaneous *XMM–Newton* and *NuSTAR* data. We updated the source ephemerides and we discuss the orbital period evolution over a baseline of almost 17 yr. The spectral analysis of these data will be reported elsewhere (Di Salvo et al., in preparation).

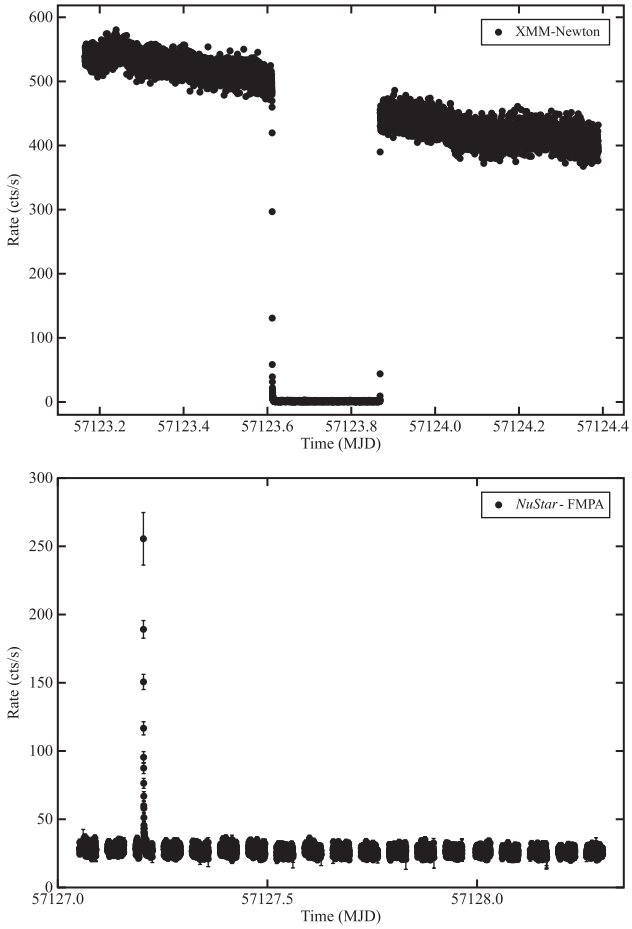

Figure 1. Light curves of the observations analysed in this work. (a) *XMM–Newton* PN, background-subtracted light curve (0.3–10 keV) at 10 s time resolution of the 2015 outburst of SAX J1808.4−3658. The drop out in the middle of the observation is the result of $\sim$21 ks off-target pointing of the instrument. (b) *NuSTAR* FMPA, background-subtracted light curve (3–79 keV) at 10 s time resolution of the 2015 outburst of SAX J1808.4−3658. After $\sim$13 ks from the beginning of the observation the source showed an X-ray burst.

2 OBSERVATIONS AND DATA REDUCTION

2.1 *XMM–Newton*

We analysed a pointed *XMM–Newton* observation of SAX J1808.4−3658 performed on 2015 April 11 (Obs.ID. 0724490201). During the observation the European Photon Imaging Camera (EPIC)-pn camera was operated in timing mode (exposure time of $\sim$105 ks), while the Reflection Grating Spectrometer (RGS) instrument was observing in spectroscopy mode (exposure time of $\sim$80 ks). Almost in the middle of the observation ($\sim$40 ks from the beginning) the satellite experienced a problem with the pointing system resulting in an $\sim$21 ks off-target observation (see Fig. 1a), which we excluded from the analysis. For this work we focused on the EPIC-pn (PN) data that we extracted using the Science Analysis Software (SAS) v. 14.0.0 with the up-to-date calibration files, and adopting the standard reduction

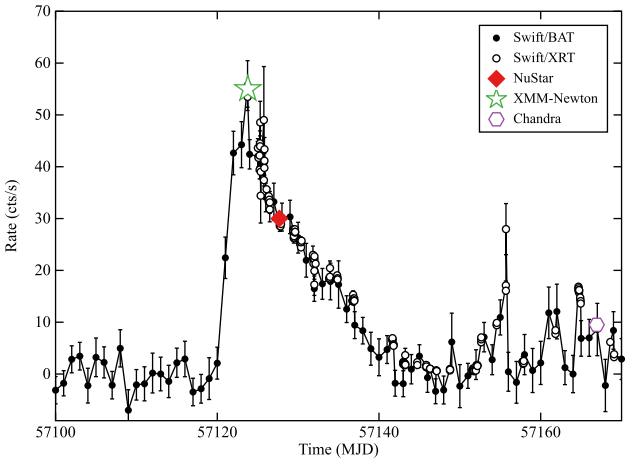

Figure 2. Light curve of the 2015 outburst of SAX J1808.4−3658 as observed by *Swift*-XRT (open-circle points) and *Swift*-BAT (black points). The green star and the red diamond represent the observations collected by *XMM–Newton* and *NuSTAR*, respectively. The purple hexagon shows the *Chandra* observation reported by Patruno et al. (2017). Count rates from the instruments have been rescaled to match *Swift*-XRT.

pipeline RDPHA (see e.g. Pintore et al. 2014, for more details on the method). We filtered the data in the energy range 0.3–10.0 keV, selecting single and double pixel events only (PATTERN ≤ 4). The average PN count rate during the observation was ∼450 counts s^{-1}, showing a clear decreasing trend from 550 counts s^{-1} at the beginning, down to 400 counts s^{-1} at the end of the observation (see Fig. 1a). We estimated a background mean count rate in the RAWX range [3:5] of the order of ∼0.6 counts s^{-1} in the energy range 0.3–10.0 keV. Moreover, we verified that the background region was not heavily contaminated by the source. No type-I burst episodes have been recorded in the PN data.

Fig. 2 shows the light curve of the 2015 outburst of the source monitored by *Swift*- X-Ray Telescope (XRT; empty-circle points) and *Swift*-Burst Alert Telescope (BAT; black points). The green star represents the *XMM–Newton* data taken roughly at the outburst peak. We corrected the PN photon arrival times for the motion of the Earth–spacecraft system with respect to the Solar system barycentre by using the BARYCEN tool (DE-405 Solar system ephemeris). We applied the best available optical position of the source (Hartman et al. 2008) listed also in Table 1.

2.2 *NuSTAR*

SAX J1808.4−3658 was observed by *NuSTAR* (Obs.ID. 90102003002) between 01:00 UT on 2015 April 15 and 07:30 UT on 2015 April 16. The red diamond in Fig. 2 shows the location of the *NuSTAR* observation with respect to the source outburst. We processed the events with the *NuSTAR* data analysis software (NUSTARDAS) version 1.5.1, resulting in an exposure time of ∼49 ks for each instrument. We filtered the source events from the FPMA and FPMB focal planes extracting a circular region of radius 100 arcsec centred at the source position. The same extracting region, but centred far from the source, has been used to extract the background. Furthermore, combining the tool NUPRODUCTS and LCMATH we extracted background-subtracted light curves for the two detectors (see Fig. 1b), characterized by an average count rate per instrument of ∼28 counts s^{-1}. During the observation a burst episode has been recorded. Solar system barycentre corrections were applied to the photon arrival times with the BARYCORR tools (using DE-405 Solar system ephemeris) as for *XMM–Newton*.

3 DATA ANALYSIS AND RESULTS

3.1 Timing analysis

Starting from the timing solution reported by Patruno et al. (2012) for the 2011 outburst of the source, we estimated the time delays $z(t)$ caused by the binary motion of the system under the hypothesis of almost circular orbits ($e \ll 1$; see Burderi et al. 2007, for more details), through the formula

$$\frac{z(t)}{c} = \frac{a \sin i}{c} \sin\left(\frac{2\pi}{P_{\rm orb}}(t - T_{\rm NOD})\right), \quad (1)$$

where $a \sin i/c$ is the projected semimajor axis of the NS orbit in light-second, $P_{\rm orb}$ is the orbital period and $T_{\rm NOD}$ is the time of passage at the ascending node. We extrapolated the starting value of the time of passage at the ascending node of the latest outburst ($T_{\rm NOD,2015}$) following the orbital evolution reported in their section 4.2 and assuming an orbital period derivative of $\dot{P}_{\rm orb,2011} = 3.5 \times 10^{-12}$ s s^{-1} (see Patruno et al. 2012, and reference therein for more details.) We then corrected the photon time of arrivals of the PN and *NuSTAR* events through the recursive formula

$$t + \frac{z(t)}{c} = t_{\rm arr}, \quad (2)$$

where t is photon emission time and $t_{\rm arr}$ is the photon arrival time to the Solar system barycentre. The correct emission times (up to an overall constant D/c, where D is the distance between the Solar system barycentre and the barycentre of the binary system) are calculated by solving iteratively the aforementioned equation (2), $t_{n+1} = t_{\rm arr} - z(t_n)/c$, with $z(t)/c$ defined as in equation (1), with the conditions $D/c = 0$, and $z(t_{n=0}) = 0$. We iterated until the difference between two consecutive steps ($\Delta t_{n+1} = t_{n+1} - t_n$) is of the order of the absolute timing accuracy of the instrument used for the observations. In our case we set $\Delta t_{n+1} = 1$ μs.

Following the most updated long-term spin frequency evolution of SAX J1808.4−3658 (Patruno et al. 2012), we looked for pulsations performing epoch folding search techniques of the whole observations using 16 phase bins, and starting with the spin frequency value $\nu_0 = 400.97520998$ Hz. We explored the frequency space around ν_0 with steps of 10^{-8} Hz, for a total of 1001 steps. We found X-ray pulsation in both the PN and the *NuSTAR* observations at a mean frequency of $\nu = 400.9752090(1)$ and $400.975214(1)$ Hz, respectively. To estimate the error on the spin frequency we performed Monte Carlo simulations generating 100 data sets with the same properties of the real data such as, length, count rate, pulsation fractional amplitude and orbital modulation. Applying the method previously described we derived a mean frequency value for each simulated data set. We defined the 1σ uncertainty interval as the standard deviation of the spin frequency distribution from the simulation.

For the *NuSTAR* data set, we repeated the analysis excluding the X-ray burst detected during the observation. We did not observe significant variation in terms of detectability of the pulse profile. Moreover, we investigated the presence of the coherent pulsation during the X-ray burst, finding evidence of X-ray pulsation with a statistical significance of $\sim 4\sigma$ consistent within errors with the average spin frequency value of the *NuSTAR* observation reported in Table 1. We decided not to exclude the X-ray burst from the timing

Table 1. Orbital parameters of SAX J1808.4−3658 combining the timing analysis of the *XMM–Newton* and *NuSTAR* observations from the 2015 outburst of the source. The reference epoch for the solution is $T_0 = 57123.1$ MJD. Spin frequency and spin frequency derivative estimates are obtained by fitting independently the two observations. Errors are at 1σ confidence level. The reported X-ray position of the source has a pointing uncertainty of 0.15 arcsec (Hartman et al. 2008).

Parameters	*XMM–Newton*	*NuSTAR*
RA (J2000)	$18^{\rm h}08^{\rm m}27\overset{\rm s}{.}62$	
Dec. (J2000)	$-36^\circ58'43\overset{''}{.}3$	
Orbital period $P_{\rm orb}$ (s)	7249.143(4)	
Projected semimajor axis $a \sin i/c$ (light-second)	62.810(3)	
Ascending node passage $T_{\rm NOD}$ (MJD)	57123.060218(3)	
Eccentricity (e)	$<4 \times 10^{-4}$	
χ^2/d.o.f.	1126.2/696	
Fundamental		
Spin frequency ν_0 (Hz)	400.9752089(1)	400.975214(1)
χ^2/d.o.f.	184.4/11	706.9/6
Spin frequency ν_0 (Hz)	400.9752075(2)	400.975208(2)
Spin frequency first derivative $\dot{\nu}_0$ (Hz s^{-1})	$2.6(3) \times 10^{-11}$	$1.1(3) \times 10^{-10}$
χ^2/d.o.f.	20.1/10	333.8/5
Second harmonic		
Spin frequency ν_0 (Hz)	400.9752098(1)	400.975213(1)
χ^2/d.o.f.	5.5/11	46.3/5
Spin frequency ν_0 (Hz)	400.9752094(4)	400.975208(3)
Spin frequency first derivative $\dot{\nu}_0$ (Hz s^{-1})	$7(7) \times 10^{-12}$	$0.9(5) \times 10^{-10}$
χ^2/d.o.f.	5.1/10	19.9/3

analysis of the source. Although intriguing, a detailed analysis of the X-ray burst properties is beyond the scope of this work.

We investigated, separately for *XMM–Newton* and *NuSTAR*, the timing properties of the source by studying the evolution of the pulse phase delays computed on time intervals of approximately 200 s. We epoch folded each segment in 16 phase bins at the spin frequency $\nu = 400.9752091$ Hz corresponding to the mean spin frequency during the PN observation with respect to the epoch $T_0 = 57123.1$ MJD. We modelled each pulse profile with a sinusoid of unitary period to determine the corresponding sinusoidal amplitude and the fractional part of phase residual. We selected only folded profiles with ratio between the sinusoidal amplitude and the corresponding 1σ error larger than 3. We detected pulsations on ∼80 and ∼60 per cent of the intervals created from the PN and *NuSTAR* observations, respectively. We tried to fit the pulse profiles including a second harmonic component, but this component resulted statistically significant only in a small fraction of intervals (∼6 and ∼1 per cent of the intervals in PN and *NuSTAR*, respectively). The fractional amplitude of the signal varies between ∼4 and ∼6 per cent, with a mean value of ∼4.5 per cent for the PN observation, while for *NuSTAR* it varies between ∼5.5 and ∼10 per cent, with a mean value of ∼8 per cent.

To determine a more accurate set of ephemeris we performed timing analysis of the combined set of PN and *NuSTAR* observations by fitting the time evolution of the pulse phase delays with the following models:

$$\begin{cases} \Delta\phi_{\rm PN}(t) = \sum_{n=0}^{3} \frac{C_n}{n!}(t - T_0)^n + R_{\rm orb}(t), \\ \Delta\phi_{\rm NS}(t) = \sum_{n=0}^{7} \frac{D_n}{n!}(t - T_0)^n + R_{\rm orb}(t), \end{cases} \quad (3)$$

where the first element of both equations represents a polynomial function used to model phase variations superposed to the residual orbital modulation $R_{\rm orb}(t)$ caused by differences between the *real* set of orbital parameters and those used to correct the photon time of arrivals (see e.g. Deeter, Boynton & Pravdo 1981). The order of the polynomial function varied between the data sets depending on the fluctuations of the pulse phases. We note that no phase-lock timing analysis of the *XMM–Newton* and *NuSTAR* data sets has been possible given the low accuracy of the timing solutions from the single observations combined with the temporal gap between them (∼3 d). Furthermore, the presence of a time drift on the internal clock of the *NuSTAR* instrument (Madsen et al. 2015), which affects the observed coherent signal making the spin frequency value significantly different compared to the PN, represents a strong limitation on the phase-connected variability timing techniques. We then emphasize that the two models in equation (3) only share the same orbital parameters component $R_{\rm orb}(t)$, meaning that the orbital parameters will be linked during the fit of the two data sets. This method has the advantage (with respect to model each observation separately) to improve the accuracy of parameters such as the orbital period and the time of passage to ascending node. If a new set of orbital parameters is found, photon time of arrivals is corrected using equation (1) and pulse phase delays are created and modelled with equation (3). We repeated the process until no significant differential corrections were found for the parameters of the model. We reported the best-fitting parameters in Table 1, while in Fig. 3 we showed the pulse phase delays of the two instruments with the best-fitting models (top panel), and the residuals with respect to the models (bottom panel). The value of $\tilde{\chi}^2 \sim 1.62$ (with 696 degrees of freedom) shows that the model well fits the pulse phase delays. However, the large distribution of the residuals from the *NuSTAR* observation (bottom right-hand panel) clearly shows the presence of a peculiar timing noise in these data, likely ascribable to the instrumental issue mentioned before (Madsen et al. 2015).

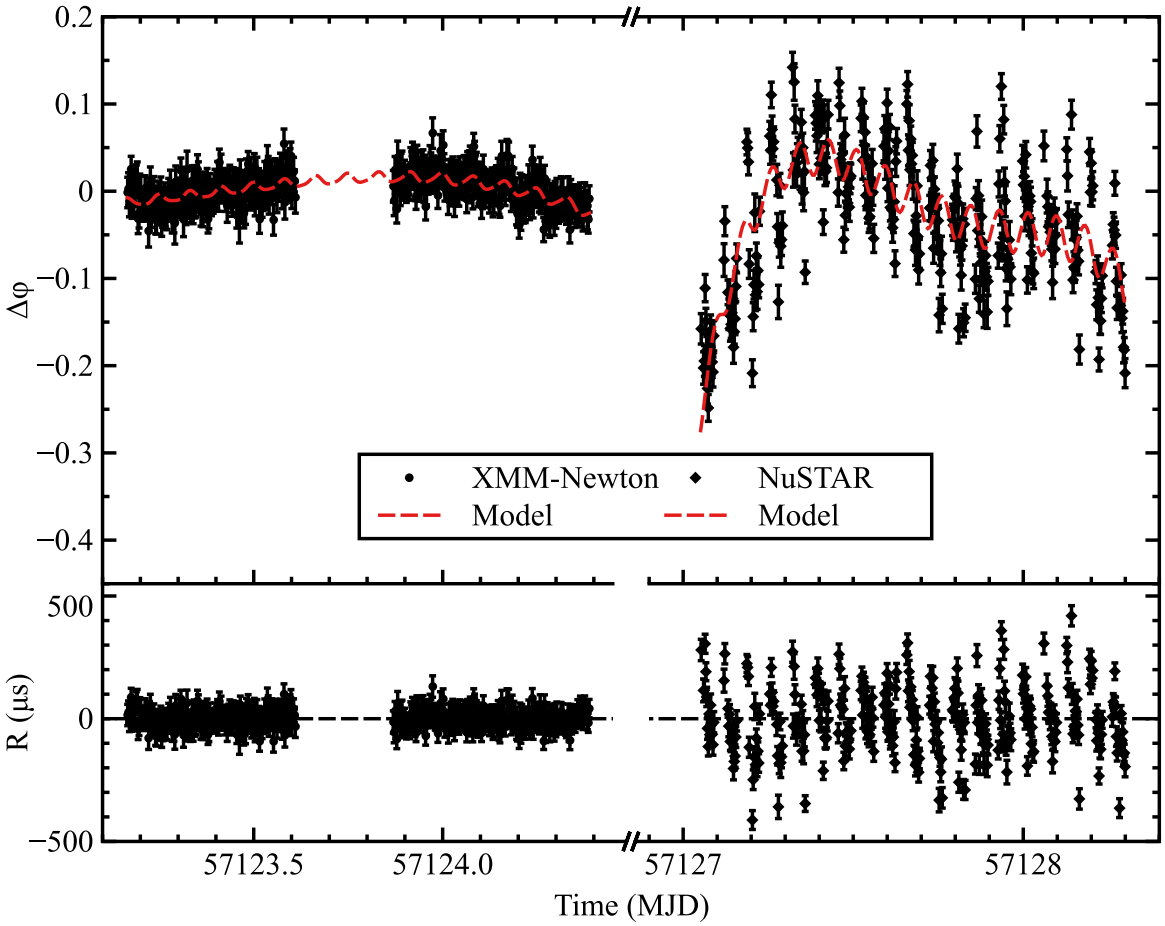

Figure 3. Top panel: pulse phase delays as a function of time computed by epoch folding the *XMM–Newton* and *NuSTAR* observations at the spin frequency $\nu_0 = 400.97520998$ Hz, together with the best-fitting model (red dotted line, see text). Bottom panel: residuals in μs with respect to the best-fitting orbital solution.

With the updated set of ephemerides reported in Table 1, we corrected the events of the PN and *NuSTAR* observations. We then epoch folded, for each observation, long intervals of data (between one and two orbital periods, depending on the statistics of the data) in order to have pulse profiles with significant fundamental and second harmonic components. To investigate the evolution of the spin frequency we fitted the pulse phase delays as a function of time with the expression

$$\Delta\phi(t) = \phi_0 + \Delta\nu\,(t - T_0) + \frac{1}{2}\dot{\nu}\,(t - T_0)^2, \tag{4}$$

where ϕ_0 is a constant phase, $\Delta\nu = (\nu_0 - \nu)$ represents the difference between the frequency at the reference epoch and the spin frequency used to epoch fold the data, $\dot{\nu}$ is spin frequency derivative and T_0 represents the reference epoch for the timing solution. For each observation, we modelled with equation (4) the phase delays obtained from both the fundamental and the second harmonic components. We reported the best-fitting parameters in Table 1, while in Figs 4(a) and (b) we showed the pulse phase delays with the best-fitting models for PN and *NuSTAR*, respectively. In Table 1 we also reported the mean spin frequency values obtained by modelling the phase delays of the fundamental component with a constant model. We measured significant spin frequency derivative values from the phase delays of the fundamental component of both the data set with values of $2.6(3) \times 10^{-11}$ and $1.1(3) \times 10^{-10}$ Hz s^{-1} for PN and *NuSTAR*, respectively. Moreover, it is worth noting that the PN data set (Fig. 4a) shows a clear mismatch between the time evolution of the fundamental and second harmonic components, while in *NuSTAR* (Fig. 4b) the two components show an overall behaviour consistent within errors.

Taking into account the uncertainties on the source position, we estimated the systematic uncertainties induced on the spin frequency correction $\delta\nu$, and the spin frequency derivative $\dot{\nu}$. Using the expression of the residuals induced by the motion of the Earth for small uncertainties on the source position δ_λ and δ_β expressed in ecliptic coordinates λ and β (see e.g. Lyne & Graham-Smith 1990), we derived the expressions $\sigma_{\nu_{\rm pos}} \leq \nu_0\, y\, \sigma_\gamma (1 + \sin^2\beta)^{1/2} 2\pi/P_\oplus$ and $\sigma_{\dot{\nu}_{\rm pos}} \leq \nu_0\, y\, \sigma_\gamma (1 + \sin^2\beta)^{1/2} (2\pi/P_\oplus)^2$, where $y = r_{\rm E}/c$ is the semimajor axis of the orbit of the Earth in light-second, $P_\oplus$ is the Earth orbital period and σ_γ is the positional error circle. Considering the positional uncertainty of 0.15 arcsec reported by Hartman et al. (2008), we estimated $\sigma_{\nu_{\rm pos}} \leq 1 \times 10^{-10}$ Hz and $\sigma_{\dot{\nu}_{\rm pos}} \leq 2 \times 10^{-17}$ Hz s^{-1}, respectively. We added in quadrature these systematic uncertainties to the statistical errors of ν_0 and $\dot{\nu}$ estimated from the timing analysis.

Finally, we investigated the properties of the pulse profile as a function of energy, dividing the PN energy range between 0.3 and 10 keV into 38 intervals, and the *NuSTAR* energy range between 1.6 and 80 keV in 10 intervals. We adjusted the width of the energy bins in order to be able to significantly detect the pulsation. We modelled

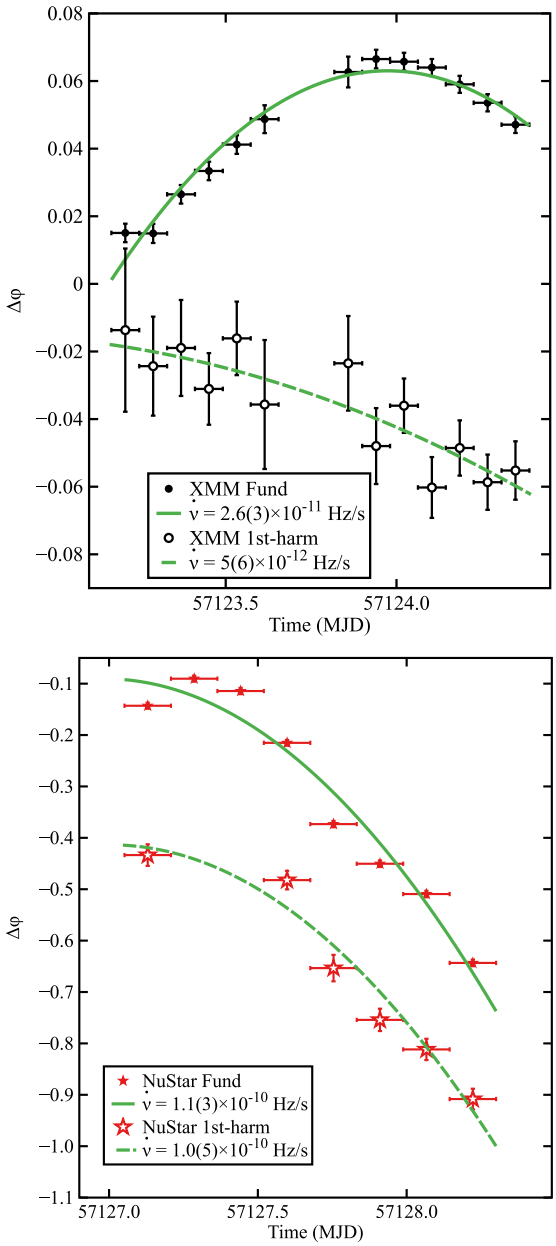

Figure 4. Time evolution of the pulse phase delays for the two data sets and corresponding best-fitting models. (a) *XMM–Newton*: pulse phase delays as a function of time for the fundamental (black filled dots) and the second harmonic (black empty dots) components of the source spin frequency. The solid and dotted green lines represent the best-fitting models for the fundamental and the second harmonic, respectively. (b) *NuStar*: pulse phase delays as a function of time for the fundamental (red filled stars) and the second harmonic (red empty stars) components of the source spin frequency. The solid and dotted green lines represent the best-fitting models for the fundamental and the second harmonic, respectively.

the background-subtracted pulse profile with two sinusoidal components (fundamental and second harmonic) for which we calculated the fractional amplitudes for each energy selection. Fig. 5 shows the dependence of the fractional amplitude of the pulse profile as a function of energy. The PN fractional amplitude of the fundamental component increases from ∼1 per cent at around 0.4 keV up to ∼7 per cent at 5 keV, after that it starts decreasing reaching the value of ∼6 per cent at 10 keV. It is interesting to note that, in

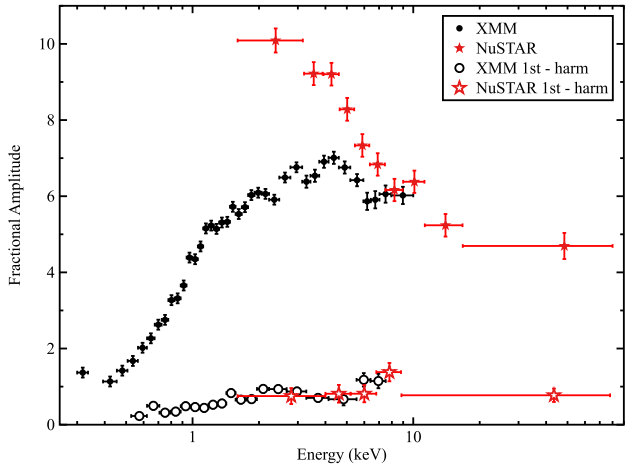

Figure 5. Evolution of the pulse profile fractional amplitude of the fundamental and first overtone used to model the pulse profile obtained from the *XMM–Newton* (black filled dots and black empty dots) and the *NuSTAR* (red filled stars and red empty stars) observations as a function of energy.

addition to the decreasing trend, the fractional amplitude seems to drop in correspondence to the iron line energy range (6.4–7 keV) (a similar behaviour has been observed during the 2008 outburst of the source, see e.g. Patruno et al. 2009a). The *NuSTAR* fractional amplitude of the fundamental component basically shows a decreasing trend between ∼10 per cent at around 2 keV and ∼5 per cent up to 80 keV. Furthermore, in Fig. 5 it can be clearly seen the discrepancy between the fundamental components (black filled points and red filled stars) of the two instruments, both in terms of maximum fractional amplitude detected and overall amplitude–energy trend observed. Differently from the fundamental, the PN second harmonic shows an increasing trend from ∼0.2 per cent at 0.5 keV up to ∼1 per cent at 10 keV. In order to significantly detect the *NuSTAR* second harmonic we created new energy selections resulting on five amplitude measurements reported with red empty stars in Fig. 5. The fractional amplitude trend is more or less constant as a function of energy around the mean value 0.7 per cent.

4 DISCUSSION

We have presented an updated timing solution for the AMXP SAX J1808.4−3658 obtained from the timing analysis of the *XMM–Newton* and *NuSTAR* observations of its 2015 outburst. The new set of orbital parameters is compatible within the errors with the timing solution obtained from the analysis of the *Chandra* observation of the same outburst reported by Patruno et al. (2017).

4.1 Secular spin evolution

As mentioned in the previous sections, the source has been observed in outburst seven times since its discovery (see e.g. Hartman et al. 2008, 2009b; Burderi et al. 2009; Patruno et al. 2012, 2017). To evaluate its secular spin frequency variation we started by considering the six constant pulse frequencies estimated from the outbursts between 1998 and 2011 (reported by Patruno et al. 2012, see their fig. 2, bottom panel) and shown in the top panel of Fig. 6 (black points). In addition we plotted the spin frequency measurements obtained from the timing analysis of the pulse phases of the fundamental component from the 2015 outburst obtained with *XMM–Newton* (blue point) and *NuSTAR* (green point). Both values significantly deviate

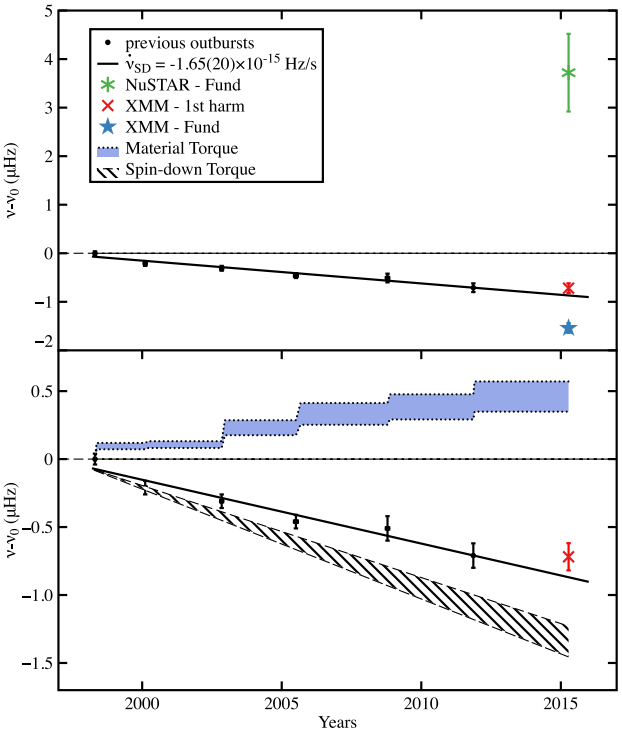

Figure 6. Top panel: secular evolution of the spin frequency of SAX J1808.4−3658 for the 1998–2015 baseline. Black points represent the frequency measurements of the previous outbursts reported by Patruno et al. (2012). Green and blue points represent, respectively, the *NuSTAR* and *XMM–Newton* frequency measurements during the 2015 outburst relative to the fundamental component of the X-ray pulsation. The red point represents the frequency measurement relative to the second harmonic component of the X-ray pulsation observed by *XMM–Newton*. Frequencies are rescaled relative to value from the 1998 outburst ($\nu_0 = 400.97521052$ Hz). Solid line represents the best-fitting model of the spin frequency values observed in the outbursts between 1998 and 2011 reported by Patruno et al. (2012). Errors are reported at 1σ confidence level. Bottom panel: schematic representation of the spin-up and spin-down effects acting on the NS spin frequency caused by the material torque and the rotating magnetic dipolar torque during the outbursts of SAX J1808.4−3658. Blue shaded region represents the spin-up effect caused by the material torque calculated assuming magnetic channelling in the accretion disc truncated at the NS radius and at the corotation radius. The hatched region represents the hypothetical magnetic dipolar spin-down effect required to describe the measured spin-down effect (black solid line) after taking into account the spin-up from the material torque.

from the expected trend drawn from the secular evolution of the previous outbursts (black solid line). The frequency discrepancy shown by *NuSTAR* most likely represents an artefact that originates from the time drift of the internal clock of the instrument (see e.g. Madsen et al. 2015). The presence of a spurious spin frequency derivative, discussed in the previous section and reported in Fig. 4(b), can significantly change the spin frequency measurements explaining the large discrepancy with respect to both the quasi-simultaneous spin frequency obtained with *XMM–Newton* and the secular evolution predicted from the previous outbursts. A large discrepancy is also observed for the spin frequency value obtained from the fit of the pulse phase fundamental component (ignoring spin frequency derivatives) of the *XMM–Newton* observation. However, we note that, as reported in Fig. 4(a), a large spin-up is detected from the analysis of this component within the ∼105 ks of exposure. This value is almost two order of magnitude larger with respect to the value reported by Burderi et al. (2006) for the 2002 outburst of the source, as well as to the upper limits reported for the other outbursts (see e.g. Hartman et al. 2008, 2009b; Patruno et al. 2012). Interestingly, we note that the frequency estimated from the timing analysis of the second harmonic component (red point) is significantly inconsistent with that estimated from the fundamental component and it falls very close (less than 2σ) from the predicted secular evolution. Moreover, contrary to the fundamental component, no significant spin frequency derivative is detectable (with a 3σ upper limit of 2.3×10^{-11} Hz s^{-1}, see Fig. 4a). The different time evolution between the fundamental and the first overtone of the pulse phase delays of SAX J1808.4−3658 has been already reported and extensively discussed for the previous outbursts of the source (see e.g. Burderi et al. 2006; Hartman et al. 2008; Patruno, Wijnands & van der Klis 2009c), however, no general agreement has been reached regarding the mechanism behind this phenomenon. We suggest that both the frequency shift and the unusually large spin frequency derivative observed from the analysis of the pulse phase fundamental component are connected to the known phase-jumping phenomenon, which most likely does not represent a real evolution of the NS spin (see e.g. Patruno et al. 2009c; Riggio et al. 2011). Although very intriguing, this subject is quite complex and requires extensive discussions that fall outside the focus of this work and they will be properly investigated in a follow-up project.

To investigate the secular spin evolution of SAX J1808.4−3658, we then consider as a good proxy of the spin frequency at the beginning of the 2015 outburst, the value estimated from the analysis of the pulse phase delays second harmonic component. We modelled the seven spin frequency values with a linear function. From the fit we obtain a $\chi^2 = 8.1$ with 5 d.o.f. and a spin frequency derivative of $\dot{\nu} = -1.5(2) \times 10^{-15}$ Hz s^{-1}, consistent with the value reported by Patruno et al. (2012). Equating the rotational-energy loss rate to the rotating magnetic dipole emission, we can infer the strength of the magnetic field at the NS polar caps. Following Spitkovsky (2006) and assuming a rotating dipole in the presence of matter, we can express the NS magnetic dipole moment as

$$\mu \simeq 1.03 \times 10^{26} \left(\frac{1}{1+\sin^2\alpha}\right)^{-1/2} I_{45}^{1/2} \nu_{401}^{-3/2} \dot{\nu}_{-15}^{1/2}\,\mathrm{G\,cm^3}, \qquad (5)$$

where α is the angle between the rotation and magnetic axes, I_{45} is the moment of inertia of the NS in units of 10^{45} g cm^2, ν_{401} is the NS spin frequency in units of 401 Hz, $\dot{\nu}_{-15}$ is the spin-down frequency derivative in units of 10^{-15} Hz s^{-1}. As suggested by Poutanen & Gierliński (2003), the shape of the pulse profiles investigated during the 1998 outburst seems to favour a small misalignment between the magnetic hotspot and the rotational pole, with the angle α ranging between 5° and 20°. Combining the constraints on the magnetic field geometry with our estimates of the spin frequency and its secular spin-down derivative, we can constrain the NS magnetic moment in the range $1.4 \times 10^{26} < \mu < 1.5 \times 10^{26}$ G cm^3. Adopting the Friedman–Pandharipande–Skyrme (FPS) equation of state (see e.g. Friedman & Pandharipande 1981; Pandharipande & Ravenhall 1989) for a 1.4 M$_\odot$ NS, we estimate a NS radius of $R_{NS} = 1.14 \times 10^6$ cm. Defining the magnetic field strength at the magnetic caps as $B_{PC} = 2\mu/R_{NS}^3$, we obtain the magnetic field ranging $1.9 \times 10^8 < B_{PC} < 2 \times 10^8$ G, which is consistent with the value reported by Patruno et al. (2012) and also consistent with the value estimated from the detection of a relativistically broadened iron line during the 2008 outburst ($B_{PC} = 2$–4×10^8 G; see e.g. Cackett et al. 2009; Papitto et al. 2009). On the other hand, this value is almost a factor of 2 smaller compared with the magnetic field estimated by Burderi et al. (2006) from the spin-down torque measured at the final stages of the 2002 outburst of the source.

It is worth noting that, even though SAX J1808.4−3658 accreted matter during the latest seven monitored outbursts, the overall secular spin evolution clearly shows a modest slowdown of the NS. Assuming standard accretion torque theory (see e.g. Pringle & Rees 1972), starting from the amount of matter accreted on to the NS surface during an outburst, we can estimate the spin variation during the outbursts. We can define the spin frequency variation due to the accreting torque as

$$\Delta\nu = \frac{\Delta M\sqrt{Gm_1 R_{\rm IN}}}{2\pi I}, \quad (6)$$

where ΔM represents the amount of matter accreted on to the NS, m_1 and I represent the mass and the moment of inertia of the NS, respectively, and $R_{\rm IN}$ is the disc radius at which the matter is channelled by the magnetic field lines and forced to accrete on to the NS magnetic poles. A rough estimate of the spin-up variation can be obtained considering $\Delta M \simeq \Delta E_{\rm bol}(Gm_1/R)^{-1}$, where $\Delta E_{\rm bol}$ represents the amount of energy released by SAX J1808.4−3658 during each outbursts. To quantify the spin frequency shift occurred between the beginning of the 1998 and the 2015 outbursts (same interval used to quantify the spin-down derivative), we consider the amount of energy released in the six outbursts happened in between. Combining the X-ray light curves reported in literature (see e.g. Hartman et al. 2008, 2009b; Patruno et al. 2012) and assuming that no outburst has been missed, we can estimate the energy released during the outburst activity of SAX J1808.4−3658 between 1998 and 2015 as $\Delta E_{\rm bol} \simeq 3.2 \times 10^{43}$ erg. The latter value has been inferred assuming a source distance of $d = 3.5$ kpc (Galloway & Cumming 2006) and a bolometric correction factor of 2.12 (see e.g. Hartman et al. 2008, and references therein) to derive the bolometric luminosity from the observed X-ray luminosity. Moreover, we considered as possible extreme values of the truncation disc radius during the outburst phase, the NS radius $R_{\rm NS} = 1.14 \times 10^6$ cm and the corotation radius $R_{\rm CO} = 3.08 \times 10^6$ cm (radius at which the Keplerian frequency equals the NS spin frequency). We then estimated that the frequency spin-up caused by the material torque of the 1998–2011 outbursts ranges between ∼0.35 and ∼0.56 μHz. In Fig. 6 (bottom panel), the blue shaded region represents the time evolution of the spin frequency as a consequence of the angular momentum accreted during the outburst phases of the source. If the material torque described above is correct, we should re-evaluate the spin-down torque acting on to the NS. Assuming the magnetic dipole radiation emission during the X-ray quiescence as the main driver of the NS spin-down, the spin-down derivative can be estimated combining the observed secular frequency shift (almost −0.8 μHz over 17 yr of observations) with that caused by the material torque (ranging between 0.35 and 0.56 μHz, considering the NS radius and the corotation radius as possible truncation radii of the disc). The spin-down derivative required to compensate the estimated spin-up material torque and to produce the observed spin-down effect should range between -2.2×10^{-15} and -2.7×10^{-15} Hz s^{-1}, a factor of almost 1.5 and 1.8 higher, respectively, than the spin-down frequency derivative estimated ignoring the material torque. Using equation (5) and adopting the FPS equation of state previously described, we can estimate the NS dipole magnetic moment, hence the magnetic field at the magnetic caps in the range $2.2 \times 10^8 < B_{\rm PC} < 3 \times 10^8$ G, very similar to the value suggested by Burderi et al. (2006). However, we note that other mechanisms such as magnetic propeller torque and gravitational radiation torque (see e.g. Hartman et al. 2008, and references therein for more details) could contribute to the spin-down torque required to describe the observed secular spin evolution of SAX J1808.4−3658.

4.2 Pulse energy dependence

SAX J1808.4−3658 shows an interesting behaviour of its pulse profile as a function of energy. As shown in Fig. 5, the pulse fractional amplitude estimated from the fundamental component varies significantly between the *XMM–Newton* and the *NuSTAR* observations of the source. We can exclude instrumental effects between the two satellites to explain such a discrepancy. Indeed, phase-coherence analyses on almost simultaneous *XMM–Newton* and *NuSTAR* have been carried out on other sources (see e.g. Sanna et al. 2017, for the AMXP IGR J00291+5934) and they did not show any peculiar difference between the two detectors. Therefore, a possible explanation may be a significant source state variation occurred in the 3 d gap between the two observations. A detailed study of this phenomenon is beyond the scope of this work, however, further investigations on the subject will be reported in a follow-up paper focusing on the spectral properties of SAX J1808.4−3658 during its 2015 outburst (Di Salvo et al., in preparation).

The peculiar trend showed by the fundamental component is consistent with that observed by the *Rossi X-ray Timing Explorer* during the 1998 outburst while it significantly differs from that of the 2002 (see e.g. Cui, Morgan & Titarchuk 1998; Falanga & Titarchuk 2007; Hartman, Watts & Chakrabarty 2009a). A similar behaviour has been observed for the other AMXPs such as IGR J00291+5934 (Falanga et al. 2005; Sanna et al. 2017), IGR J17511−3057 (Papitto et al. 2010) and XTE J1751−305 (Falanga & Titarchuk 2007), although for the latter a good coverage of the trend below 4 keV is lacking. On the other hand, the constant energy dependence of the fractional amplitude inferred from the second harmonic component seems to remain unvaried over the outbursts (see e.g. Cui et al. 1998; Hartman et al. 2009a). The mechanism responsible for the complex energy spectrum observed for the AMXPs fractional amplitude is still under discussion, however, processes such as strong Comptonization of the beamed radiation have been proposed to explain the hard spectrum of the pulsation observed in several systems (see e.g. Falanga & Titarchuk 2007). Alternatively, Muno, Özel & Chakrabarty (2002, 2003) proposed the presence of a hotspot region emitting as a blackbody with a temperature significantly different with respect to the neutron star surface as the mechanism responsible for the increasing pulse amplitude with energy in the observer rest frame, compatible to what observed for systems such as Aql X-1 (Casella et al. 2008), Swift J1756.9−2508 (Patruno, Altamirano & Messenger 2010), XTE J1807−294 (Kirsch et al. 2004) and SAX J1748.9−2021 (Patruno et al. 2009b; Sanna et al. 2016).

4.3 Orbital period evolution

During the last 17 yr SAX J1808.4−3658 has been detected in outburst seven times, and for each of these phases an accurate set of ephemerides has been produced. In order to investigate the evolution of the orbital period of the source we study the correction on the NS passage from the ascending node $\Delta T_{\rm NOD}$ (with respect to the beginning of the 1998 outburst) for each outburst, as a function of the orbital cycles elapsed from the reference time (see top left-hand panel in Fig. 7). $\Delta T_{\rm NOD}$ represents the difference between the predicted passage from the ascending node $T_{\rm NOD,predict} = T_{\rm NOD,1998} + N P_{\rm orb_{1998}}$ and the reference value $T_{\rm NOD,1998}$, where the integer N is the number of orbital cycles elapsed between two different $T_{\rm NOD}$. We started by fitting the data with a quadratic function:

$$\Delta T_{\rm NOD} = \delta T_{\rm NOD,1998} + N\,\delta P_{\rm orb_{1998}} + 0.5\,N^2\,\dot{P}_{\rm orb}\,P_{\rm orb_{1998}}, \quad (7)$$

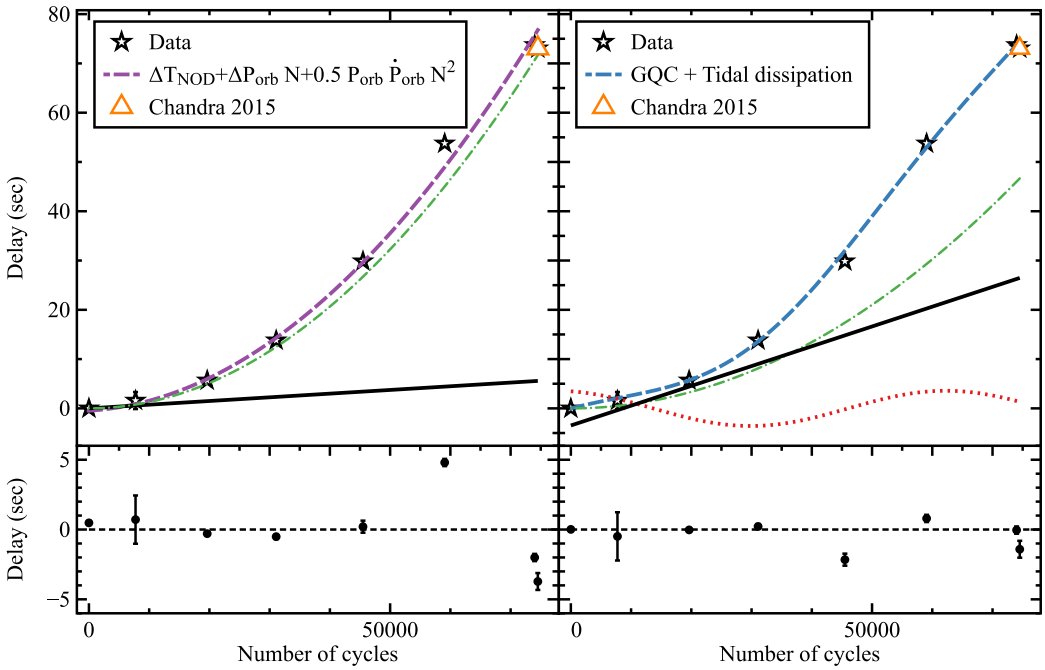

Figure 7. Top left-hand panel: differential correction $\Delta T_{\rm NOD}$ to the time of passage at the ascending node for the seven outbursts shown by SAX J1808.4−3658. Each point is computed with respect to the beginning of the first outburst occurred in 1998 (see Section 4.3 for more details). The dashed purple line represents the best-fitting quadratic model used to fit the data. Dot-dot-dot–dashed black line and dot–dashed green line represent the linear and the quadratic components of the model, respectively. Bottom left-hand panel: residuals with respect to the best-fitting quadratic model. Top right-hand panel: same differential correction $\Delta T_{\rm NOD}$ shown in the left-hand panel, but fitted with the gravitational quadrupole coupling (GQC) model powered by a tidal dissipation mechanism (blue). Dot-dot-dot–dashed black line, dot–dashed green line and dotted red line represent the linear, the quadratic and the sinusoidal components of the model, respectively. Bottom right-hand panel: residuals with respect to the GQC model powered by a tidal dissipation mechanism. For comparison we reported the value $T_{\rm NOD}$ from the 2015 outburst reported by Patruno et al. (2017).

Table 2. SAX J1808.4−3658 best-fitting orbital parameters derived combining the seven outbursts observed between 1998 and 2015. All parameters are referred to the 1998 outburst, with $T_{\rm NOD,1998} = 50914.794528(2)$ (MJD) and $P_{\rm orb,1998} = 7249.156444(23)$ s (Burderi et al. 2009). Uncertainties are reported at 1σ confidence level. Uncertainties are scaled by a factor $\sqrt{\tilde{\chi}^2}$.

Parameters	Value
Ascending node passage $T_{\rm NOD}$ (MJD)	50914.79452(1)
Orbital period $P_{\rm orb}$ (s)	7249.15651(9)
Orbital period derivative $\dot{P}_{\rm orb}$ (s s^{-1})	$3.6(4) \times 10^{-12}$
χ^2/d.o.f.	429.5/4

where the correction to the adopted time of passage from the ascending node, $\delta T_{\rm NOD,1998}$, the correction to the orbital period, $\delta P_{\rm orb_{1998}}$, and the orbital period derivative, $\dot{P}_{\rm orb}$, are the fit parameters. Statistically speaking, the fit is not acceptable, since a $\chi^2 = 429.5$ (for 4 degrees of freedom) corresponds to a probability of obtaining a larger χ^2 of $\sim 2.4 \times 10^{-6}$ (largely below the conventional accepted 5 per cent threshold). In Table 2 we reported the updated orbital parameters inferred from the best-fitting model. To take into account the large value of the reduced $\tilde{\chi}^2$ obtained from the fit, we rescaled the uncertainties of the fit parameters by the quantity $\sqrt{\tilde{\chi}^2}$. We investigated the presence of an orbital period second derivative (as suggested by Patruno et al. 2012) by adding a cubic term in equation (7). The fit with the updated model is statistically unacceptable, with $\chi^2_\nu = 173.3$ for 3 d.o.f. (p-value probability of $\sim 1 \times 10^{-6}$). Moreover, with a null hypothesis probability of ~ 0.07, we note that the χ^2 variation caused by introducing the new component ($\Delta\chi^2 \sim 256$ for 1 d.o.f) is not statistically significant for the specific model. We therefore ignored it for the following discussion. As we can see from the residuals reported in the bottom left-hand panel of Fig. 7, the farthest outlier (more than 30σ) from the best-fitting quadratic model corresponds to the 2011 outburst ($\sim$59 000 orbital cycles) from which Patruno et al. (2012) inferred the time second derivative of the orbital period. Removing this outburst lowers the χ^2_ν to $\sim$9.6 (with 3 d.o.f.), consistent with a constant orbital period derivative of $\dot{P}_{\rm orb} = 3.56(6) \times 10^{-12}$ s s^{-1}. Both values of $\dot{P}_{\rm orb}$ inferred from the analysis (with or without the 2011 outburst) are compatible within errors with the estimates reported by Di Salvo et al. (2008) and Hartman et al. (2008) for the orbital evolution of the source up to the 2005 outburst, and with the estimates of Hartman et al. (2009b) and Burderi et al. (2009) up to the 2009 outburst.

The origin of the observed $\dot{P}_{\rm orb}$ is still not fully understood, yet different possible mechanisms have been proposed over the years (see e.g. Di Salvo et al. 2008; Hartman et al. 2008; Burderi et al. 2009; Patruno et al. 2012). However, there is consensus on the fact that conservative mass transfer is not compatible with the observed value of $\dot{P}_{\rm orb}$ for SAX J1808.4−3658. This can be easily demonstrated by estimating the mass-loss rate from the secondary as a function of the observed orbital period derivative. Combining Kepler's third law with the condition for mass transfer via Roche lobe overflow ($\dot{R}_{\rm L2}/R_{\rm L2} = \dot{R}_2/R_2$, where the $R_{\rm L2}$ and R_2 are the Roche lobe radius and radius of the secondary, respectively), we can write the averaged secondary mass-loss rate as (see Burderi et al. 2010, for further details on the derivation of the expression)

$$\dot{m}_2 = 1.2\,(3n-1)^{-1}\, m_{2,0.14\odot} \left(\frac{\dot{P}_{\rm orb,-12}}{P_{\rm orb,2\,h}}\right) \times 10^{-9}\,{\rm M}_\odot\,{\rm yr}^{-1}, \quad (8)$$

where n is the index of the mass–radius relation of the secondary $R_2 \propto M_2^n$, $m_{2,0.14\odot}$ is the mass of the companion star in units of 0.14 $M_\odot$ (from the mass function it can be inferred that $m_2 \leq 0.14\ M_\odot$ at 95 per cent confidence level; see e.g. Chakrabarty & Morgan 1998), $\dot{P}_{\rm orb,-12}$ is the orbital period derivative in units of 10^{-12} s s^{-1} and $P_{\rm orb,2\,h}$ is the orbital period in units of 2 h (appropriate for SAX J1808.4−3658 since $P_{\rm orb} \approx 2.01$ h). Since the transferred mass is lost by the companion star, the quantity on the right-hand side of equation (8) must be negative, which implies a secondary mass–radius index $n < 1/3$. Assuming a fully convective companion star ($n = -1/3$), we find $\dot{m}_2 \simeq -2 \times 10^{-9}\ M_\odot\ {\rm yr}^{-1}$. The conservative mass transfer scenario implies that mass transferred during the outburst must be completely accreted by the NS, while no mass is accreted or lost during quiescence phases. To verify whether the value inferred from equation (8) is compatible with a conservative scenario, we extrapolated the companion averaged mass-loss rate from the observed flux of the source. Combining the observations of the source during the outburst phases shown in the past 17 yr of monitoring, and taking into account that the source spends on average 30 d in outburst every 2.5 yr, we can infer the averaged mass-loss rate $\dot{m}_{2,\rm obs} \sim 2 \times 10^{-11}\ M_\odot\ {\rm yr}^{-1}$. The discrepancy of two order of magnitude between the mass-loss rate values strongly suggests that the observed orbital period derivative is not compatible with a conservative mass transfer scenario.

4.3.1 Gravitation quadrupole coupling

As noted by Hartman et al. (2008), the large orbital period derivative observed in SAX J1808.4−3658, as well as its orbital parameters, is very similar to those of a small group of black widow millisecond pulsars, such as PSR B1957+20 (Applegate & Shaham 1994; Arzoumanian et al. 1994) and PSR J2051−0827 (Doroshenko et al. 2001; Lazaridis et al. 2011; Shaifullah et al. 2016). Similar orbital period variations have been observed in the red-back system PSR J2339−0533 (Pletsch & Clark 2015), in the transitional red-back system PSR J1023+0038 (Archibald et al. 2013) and in the LMXB system EXO 0748−676 (Wolff et al. 2009).

Orbital period variations observed in these systems have been interpreted in terms of gravitational quadrupole coupling (GQC), i.e. gravitational coupling between the orbit and the variations of the quadrupole moment of the magnetically active companion star (Applegate 1992; Applegate & Shaham 1994). Applegate's GQC model proposes that magnetic fields can vary the mass distribution of an active star by transitioning different states of fluid hydrostatic equilibrium. The variable deformation of the companion is then explained as the result of the star angular momentum redistribution generated likely by a magnetic torque that causes cyclic spin-up and spin-down of the companion's outer layers. Variations of the companion oblateness will then be communicated on short (almost dynamical) time-scales by gravity to the orbit inducing orbital period changes. An increase in the quadrupole moment will cause the orbit to shrink (negative orbital period derivative), vice versa a decrease in the quadrupole moment will result in a widening of the orbit (positive orbital period derivative). We can express the variation of the orbital period in terms of the variable quadrupole moment ΔQ as

$$\frac{\Delta P_{\rm orb}}{P_{\rm orb}} = -9\frac{\Delta Q}{m_2 a^2}, \tag{9}$$

where m_2 is the companion mass and a is the orbital separation (Applegate & Shaham 1994). The variation of the quadrupole moment of the companion can be related to the change in the angular velocity ($\Delta\Omega$) of the outer layers caused by the transfer of angular momentum (ΔJ) by the relation

$$\Delta Q = \frac{2\, m_{\rm s}\, R_2^5}{9\, G\, m_2}\Omega\, \Delta\Omega, \tag{10}$$

where Ω is the star angular velocity, and R_2 and $m_{\rm s}$ represent the radius and the mass of a thin outermost shell of the companion star, respectively. Combining equations (9) and (10), and assuming that Ω is almost synchronous with respect to the orbital angular velocity, we obtain the variable angular velocity required to produce orbital period changes $\Delta P_{\rm orb}$ (Applegate & Shaham 1994):

$$\frac{\Delta\Omega}{\Omega} = \frac{G\, m_2^2}{2 R_2^3\, m_{\rm s}}\left(\frac{a}{R_2}\right)^2\left(\frac{P_{\rm orb}}{2\pi}\right)^2\frac{\Delta P_{\rm orb}}{P_{\rm orb}}. \tag{11}$$

To investigate this scenario we attempted to describe the data reported in Fig. 7 assuming the following prescription for the orbital period:

$$\Delta T_{\rm NOD} = \delta T_{\rm NOD,1998} + N\,\delta P_{\rm orb_{1998}} + A\sin\left(\frac{2\pi}{P_{\rm mod}} N\, P_{\rm orb_{1998}} + \psi\right), \tag{12}$$

where A represents the amplitude of the oscillation shown by the $\Delta T_{\rm NOD}$, $P_{\rm mod}$ is the modulation period and ψ is modulation phase. We obtained the best fit ($\chi^2_\nu = 26.7$ for 3 d.o.f.) for $\delta P_{\rm orb_{1998}} = 9.3(3) \times 10^{-4}$ s, $P_{\rm mod} = 21.1(1.8)$ yr and $A = 10.1(7)$ s. It is worth noting that the best-fitting residuals (Fig. 7, bottom panel) improved with respect to the previous model, however, the reported χ^2_ν value indicates a statistically unacceptable fit. Starting from the amplitude of the oscillation A measured from the fit of $\Delta T_{\rm NOD}$, we can infer the amplitude of the orbital period modulation via the relation

$$\frac{\Delta P_{\rm orb}}{P_{\rm orb}} = 2\pi\frac{A}{P_{\rm mod}} = 0.95(7) \times 10^{-7}. \tag{13}$$

According to Applegate & Shaham (1994), the variable part of the luminosity ΔL required to produce orbital period change $\Delta P_{\rm orb}$ is given by

$$\Delta L \simeq \frac{\pi}{3}\frac{G\, m_2^2}{R_2 P_{\rm mod}}\left(\frac{a}{R_2}\right)^2\frac{\Delta\Omega}{\Omega}\frac{\Delta P_{\rm orb}}{P_{\rm orb}}. \tag{14}$$

To quantify ΔL we made the following assumptions: (i) the thin shell that differentially rotates with respect to the companion star has a mass $m_{\rm s} \simeq 0.1 m_2$ (Applegate & Shaham 1994); (ii) we approximate the companion star Roche lobe radius as $R_{\rm L2} \simeq 0.462\,[q/(1+q)]^{1/3} a$, valid for mass ratio $q \leq 0.8$ (Paczyński 1971); (iii) the conversion efficiency of internal luminosity into mechanical energy to power the shell oscillations in the gravitational potential of the companion is of the order of 10 per cent (Applegate 1992); (iv) combining Roche lobe overflow mass transfer condition ($R_2 \simeq R_{\rm L2}$) with the binary mass function, we can express the companion mass radius as $R_2 \simeq 0.37\, m_{2,\odot}^{1/3}\, P_{\rm orb,2\,h}\ R_\odot$, where $m_{2,\odot}$ represents the companion mass in units of solar masses and $P_{\rm orb,2\,h}$ is the orbital binary period in units of 2 h. Using the aforementioned assumption in equations (11) and (14), we find the internal energy required to power the GQC mechanism:

$$L_{\rm GQC} = 1.5 \times 10^{32} m_{1,\odot}\, q^{1/3}(1+q)^{4/3} P_{\rm orb,2\,h}^{-2/3}\frac{A^2}{P_{\rm mod,yr}^3}\ {\rm erg\ s^{-1}}, \tag{15}$$

where $m_{1,\odot}$ represents the NS mass in units of solar masses and $P_{\rm mod,yr}$ is the modulation period in units of years. Substituting the parameters of SAX J1808.4−3658 in equation (15) (in particular a companion mass of 0.047 $M_\odot$ obtained assuming a NS mass of

1.4 $M_\odot$, and a binary inclination of 65° derived from the modelling of the reflection component; Di Salvo et al., in preparation), the companion star must have a source of energy capable of supplying an internal luminosity $L_{GQC} \sim 10^{30}$ erg s^{-1}.

Another important aspect that should be discussed is the magnetic field strength required to produce the orbital period variation observed in the system. Starting from the formula reported by Applegate (1992), the mean subsurface field can be expressed as

$$B \simeq 3.4 \times 10^4 (m_{1,\odot} + m_{2,\odot})^{1/3} P_{\rm orb,2\,h}^{-3/2} A^{1/2} P_{\rm mod,yr}^{-1}\ {\rm G}. \quad (16)$$

Substituting the results obtained for SAX J1808.4−3658, we estimate a mean subsurface field $B \simeq 6 \times 10^3$ G. Interestingly, similar magnetic field values have been reported by Reiners (2012) from the observation of isolated brown dwarfs and low-mass stars. In the following we analyse all the possible source of energy that could power the GQC oscillations.

4.3.2 *Source of energy to power the GQC mechanism*

(i) *Nuclear energy.* To determine the internal luminosity available in the core of the very low massive and likely old companion star of SAX J1808.4−3658, we simulated the evolution of such a star by means of stellar evolutionary code (ATON; for more details see e.g. Ventura et al. 1998; Ventura, D'Antona & Mazzitelli 2008; Tailo et al. 2015, 2016). Starting from a 1.0 $M_\odot$ star with solar chemistry, we made it lose mass at constant rate ($\dot{M} = 1.0 \times 10^{-9}$ $M_\odot$ yr^{-1}), as it evolved during the hydrogen burning phase, down to the point it reached the mass of 0.047 $M_\odot$. Subsequently we left it evolve until we were able to do so. For a companion mass of $m_2 = 0.047$ $M_\odot$, for which nuclear burning is not active anymore, we estimated a luminosity $L_2 \simeq 10^{-4.5}$ $L_\odot \simeq 1.2 \times 10^{29}$ erg s^{-1} (similar results can be obtained following the stellar properties reported in literature, see e.g. Chabrier & Baraffe 1997), almost an order of magnitude fainter than the source of energy required to power the GQC effects previously described.

(ii) *Companion star irradiation*. The optical counterpart of SAX J1808.4−3658 (V4584 Sagittarii) shows spectral properties characteristic of an evolved (mid-to-late type) star (Roche et al. 1998), likely reflecting a very low mass (irradiation-bloated) brown dwarf (see e.g. Bildsten & Chakrabarty 2001). High-time resolution CCD photometry observations of the optical counterpart during the X-ray quiescence phase of SAX J1808.4−3658 allowed to infer an optical flux of $V \sim 21.5$ mag (Homer et al. 2001). The lack of ellipsoidal variations in the flux emission combined with the observed sinusoidal binary modulation have been explained by Homer et al. (2001) as the result of the irradiation of the companion star face by a quiescence irradiating X-ray flux ($L_{\rm irr} \sim 10^{33}$ erg s^{-1}) compatible with low-level mass transfer driven by gravitational radiation losses, but incompatible with the X-ray luminosity of the source observed in quiescence, $\sim 10^{31.5}$ erg s^{-1} (Campana et al. 2002). Alternatively, Burderi et al. (2003) (see also Campana et al. 2004) proposed that the observed optical flux might originate from the illumination of the companion by the rotation-powered pulsar emission during quiescence, which switches on once the magnetospheric radius exceeds the light cylinder radius. The power released by the active magneto-dipole emitter can be expressed as $L_{\rm PSR} = 2/(3c^3)\mu^2\omega^4 \simeq 1.6 \times 10^{34} I_{45}\, \nu_{401}\, \dot{\nu}_{-15,\rm SD}$ erg s^{-1}, where I_{45} represents the NS moment of inertia in units of 10^{45} g cm^2, μ_{401} is the NS spin frequency in units of 401 Hz and $\dot{\nu}_{-15,\rm SD}$ represents the spin-down frequency derivative in units of 10^{-15} Hz s^{-1}. Substituting the value $\dot{\nu}_{-15,\rm SD} \simeq 2.5$ (see Section 4.1 for more details), we estimate a luminosity $L_{\rm PSR} \simeq 4 \times 10^{34}$ erg s^{-1}. In the hypothesis of an isotropic irradiation, only a fraction $f = (1 - \cos\theta)/2$ is intercepted by the companion star, where θ represents half of the angle subtended by the secondary as seen from the NS and it relates to the binary system by the expression $\tan\theta = R_2/a$, with R_2 and a being the companion star radius and the orbital separation, respectively. Since the companion star fills its Roche lobe, we can approximate R_2 with $R_{L2} \simeq 0.462\,[q(1+q)]^{1/3} a$ (Paczyński 1971). Assuming $m_1 = 1.4$ $M_\odot$ and $m_2 = 0.047$ $M_\odot$, we obtain that only a fraction $f \simeq 0.006$ of the pulsar luminosity will be intercepted and reprocessed by the companion star, corresponding to a luminosity of $\sim 2.4 \times 10^{32}$ erg s^{-1}. Adopting an efficiency factor of the order of 10 per cent (see Applegate & Shaham 1994, for more details) to convert the irradiation energy into mechanical energy, we estimate that the radio pulsar could potentially provide enough energy to power the observed GQC effects. However, as described by Applegate (1992), the cyclic magnetic activity that generates the variable quadrupole moment needs to be powered from the inner regions of the star. Therefore, it remains to be investigated whether the irradiation energy impinging on the companion star can be converted to internal energy. The total energy generated by the rotating magnetic dipole and intercepted by the companion, as described above, is $\sim 2 \times 10^{32}$ erg s^{-1}, characterized by a quite uncertain spectral distribution. Broadly speaking, a consistent fraction of this radiation is emitted in the form of ultralow frequency electromagnetic radiation (ULF, hereafter) at the spin frequency of the NS, namely $\sim$400 Hz. These frequency is well below the plasma frequency of the companion photosphere, $\nu_{\rm p} \simeq 7 \times 10^6 \rho^{1/2} (X + Y/2)^{1/2}$ GHz, where ρ is the density of the photosphere, and X and Y represent the hydrogen and helium mass fraction, respectively. In this situation plasma behaves has a metal almost entirely reflecting the impinging radiation (see e.g. Stenson et al. 2017), which is therefore unable to effectively penetrate the external layers of the companion and power the GQC mechanism. In line with the Goldreich and Julian model (see Goldreich & Julian 1969; Hirotani 2006 and references therein), the remaining power, still of the order of $\times 10^{32}$ erg s^{-1}, is emitted in the form of high-energy gamma-rays and electron–positron relativistic pairs. According to Hameury (1996), this energetic radiation is capable to penetrate up to a column depth of $\sim$100 g cm^{-2}, with corresponds to a physical depth well below few kilometres, i.e. less than 1×10^{-4} of the Roche lobe filling companion. This penetration is by far too shallow to power the GQC mechanism in which the displacement of the shell of matter responsible for quadrupole moment variation is of the order of a tenth of the stellar radius (Applegate 1992). Furthermore, we consider the irradiation of the companion star face as the result of the quiescence irradiating X-ray flux. According to Podsiadlowski (1991), Hameury (1996) and Hameury & Ritter (1997), the X-ray penetration on the companion star is even less than 100 g cm^{-2}. All this seems to suggest that the internal energy required to power the GQC mechanism cannot be supplied by external irradiation of the companion star.

(iii) *Tidal dissipation*. Another possible mechanism to transfer energy to the companion star is via tidal dissipation. The key ingredient for this process is the asynchronism between the binary system and the companion star. The same magnetic activity invoked to explain the variable quadrupole moment of the companion star could contribute to a torque that slows down the spin of the secondary by means of a magnetic-braking-like mechanism supported by mass loss from irradiation-driven winds powered by the pulsar emission intercepted by the companion. The torque holds the companion star out of synchronous rotation with respect to the binary system, generating a tidal torque and consequently tidal dissipation. Following equation (21) in Applegate & Shaham (1994),

to obtain a tidal luminosity of the order 10^{30} erg s^{-1} (luminosity required to power the orbital period changes previously described), the following mass-loss rate is required:

$$\dot{m}_{\rm T} = 1.16 \times 10^{-10} \left(\frac{a}{l}\right)^2 L_{30}^{1/2}\, t_{\rm syn,4}^{-1/2}\, I_{2,51}^{1/2}\, {\rm M}_\odot\, {\rm yr}^{-1}, \quad (17)$$

where (a/l) represents the ratio between the binary separation and the lever arm of the mass ejected from the companion star, L_{30} is the tidal luminosity in units of 10^{30} erg s^{-1} and $I_{2,51} = 0.1 m_2 R_{\rm L2}^2$ is the donor moment of inertia defined in units of 10^{51} g cm^2. The parameter $t_{\rm syn,4}$ represents the tidal synchronization time in units of 10^4 yr that is defined as

$$t_{\rm sys,4} = \frac{0.65}{\mu_{12}} \left(\frac{R_{\rm L2}}{R_2}\right)^6 (1+q)^2 \frac{m_{2,\odot}}{R_{2,\odot}}, \quad (18)$$

where $\mu_{12} = 3 \times 10^{12}\, L_{{\rm T},\odot}^{1/3}\, R_{2,\odot}^{-5/3}\, m_2^{2/3}$ g cm^{-1} s^{-1} is the mean dynamic viscosity with $L_{{\rm T},\odot}$ and $R_{2,\odot}$ representing the companion star luminosity and radius, respectively, all rescaled in solar units. Considering $R_2 \simeq R_{\rm L2}$ and $m_{2,\odot} = 0.047$ we find that for $L_{\rm T} \sim 10^{30}$ erg s^{-1} the synchronization time is approximately 3.5×10^3 yr. Substituting these values into equation (17) and assuming a magnetic lever arm $l \simeq 0.5a$ (in analogy with Applegate & Shaham 1994), we estimate the tidal mass loss to be of the order $\sim 1.5 \times 10^{-9}$ M$_\odot$ yr^{-1}. Interestingly, the estimated mass-loss rate is similar to the value inferred from the analysis of the NS spin-up during its 2002 outburst (Burderi et al. 2006, see however, Hartman et al. 2008 who suggest that no NS spin period derivative is observable during that outburst), and from the global parabolic trend interpreted as the orbital period derivative. In fact, a companion mass-loss rate as the one estimated must have an influence on the orbital period evolution of the system, that it is not taken into account by the GQC mechanism described by Applegate & Shaham (1994), though the consequent orbital expansion is clearly mentioned in their work. Following Burderi et al. (2009), the orbital period derivative caused by general relativity (GR) angular momentum and matter losses can be expressed as follows:

$$\dot{P}_{\rm orb,-12} = -1.38\, m_{1,\odot}^{5/3}\, q(1+q)^{-1/3} P_{\rm orb,2\,h}^{-5/3} + 0.648\, m_{1,\odot}^{-1}\, q^{-1} P_{\rm orb,2\,h}\, g(\beta, q, \alpha)\, \dot{m}_{-9}, \quad (19)$$

where q is the mass ratio between the companion and the compact object, $g(\beta, q, \alpha) = 1 - \beta q - (1-\beta)(\alpha + q/3)/(1+q)$ reflects the angular momentum losses because of mass lost from the system with β being the fraction of the mass lost by the companion star that is accreted on to the NS and $\alpha = l_{\rm ej} P_{\rm orb}\, (m_1 + m_2)^2/(2\pi a^2 m_1^2)$ the specific angular momentum of the matter leaving the system ($l_{\rm ej}$) in units of the specific angular momentum of the companion star located at a distance r_2 from the centre of mass of the system with an orbital separation a. To take into account the correlation between the GQC effects, the ejected matter required for the tidal dissipation process and its effect on the orbital evolution, we modified the model reported in equation (12) as follows:

$$\Delta T_{\rm NOD} = \delta T_{\rm NOD,1998} + N\, \delta P_{\rm orb_{1998}} + \frac{1}{2} P_{\rm orb_{1998}}\, \dot{P}_{\rm orb} + A \sin\left(\frac{2\pi}{P_{\rm mod}} N\, P_{\rm orb_{1998}} + \psi\right), \quad (20)$$

where $\dot{P}_{\rm orb}$ is fixed to the value obtained from equation (19) when inserting the mass-loss rate estimated from equation (17). This new model allows us to fit the GQC effects properly taking into account the response of the binary system caused by the ejection of the matter required to power the GQC mechanism. In the top right-hand panel of Fig. 7 we show a possible application of this model to SAX J1808.4−3658. More specifically, the best-fitting model reported here has been obtained assuming (i) a magnetic lever arm $l \simeq 0.5a$ and (ii) that matter is ejected from the system with a specific angular momentum proportional to its distance from the binary centre of mass along the line connecting the two components of the system. This assumption implies that, during the magnetic-braking-like mechanisms, the matter remains attached to the field lines for a time interval much shorter than the companion orbital period. The obtained best fit corresponds to the following parameters: $\delta P_{\rm orb_{1998}} = 4(0.7) \times 10^{-4}$ s, $P_{\rm mod} = 14.9(2.7)$ yr, $A = 3.6(6)$ s and $\dot{P}_{\rm orb} = 2.3 \times 10^{-12}$ s s^{-1}, corresponding to a mass-loss rate of $\sim 8 \times 10^{-10}$ M$_\odot$ yr^{-1}. Although statistically unacceptable ($\chi^2_\nu = 41.6$ for 3 d.o.f.), the distribution of the best-fitting residuals (Fig. 7, bottom right-hand panel) suggests that the model is potentially capable to describe the orbital evolution of SAX J1808.4−3658. However, it is worth noting that at the moment the data sample is too small to allow a self-consistent determination of all the model parameters, such as the magnetic field lever arms or the specific angular momentum of the matter ejected from the system. More outbursts of the source are therefore required to confirm the presence of periodic oscillations of the orbital period; in alternative these may be random oscillations of the orbital period around a global parabolic trend, possibly caused by random fluctuations of a non-conservative mass transfer rate.

4.3.3 Non-conservative mass transfer scenario

Di Salvo et al. (2008) and Burderi et al. (2009) proposed an alternative scenario to explain the large orbital period derivative that invokes a non-conservative mass transfer from the companion star to the NS. The idea is that even during the quiescence phases the companion star overflows its Roche lobe, but the transferred matter is ejected from the system rather than falling on to the NS surface. Using equation (5) from Di Salvo et al. (2008), the secular orbital period derivative of the system driven by emission of gravitational waves and mass loss can be expressed as

$$\dot{P}_{\rm orb} = [-0.138 m_{1,\odot}^{5/3}\, q_{0.1}(1 + 0.1 q_{0.1})^{-1/3} P_{\rm orb,2\,h}^{-5/3} + 6.84 m_{1,\odot}^{-1}\, q_{0.1}^{-1} P_{\rm orb,2\,h}\, g(\beta, q, \alpha)\, \dot{m}_{2,-9}] \times 10^{-12}\, {\rm s\, s^{-1}}, \quad (21)$$

where $q_{0.1}$ is the mass ratio in units of 0.1. Substituting equation (8) in the previous expression and using the orbital period derivative determined from the timing analysis ($\dot{P}_{\rm orb} \sim 3.6 \times 10^{-12}$ s s^{-1}), we derive a relation between the two masses of the objects forming the binary system (m_1 and m_2) and the companion mass–radius index (n). Top panel of Fig. 8 shows the mass–radius index as a function of the companion mass assuming three different NS mass values (1.2 M$_\odot$, cyan; 1.4 M$_\odot$, black; and 2.1 M$_\odot$, purple). The three functions are calculated under the assumptions that (i) the mass ejected from the system leaves the system with the specific angular momentum at the inner Lagrangian point $\alpha_{\rm L1} = [1 - 0.462(1+q)^{2/3} q^{1/3}]^2$ and (ii) the fraction of mass lost from the companion and accreted on to the NS is $\beta \sim 0.01$, roughly corresponding to the ratio between the times of X-ray activity and quiescence phase occurred since the source discovery. The range of masses displayed for the companion star has been determined from the mass function estimated from the updated ephemeris of the X-ray pulsar and assuming inclination angles between 90° and 15° (corresponding to the 95 per cent confidence level; see e.g. Chakrabarty & Morgan 1998). Moreover, the horizontal line

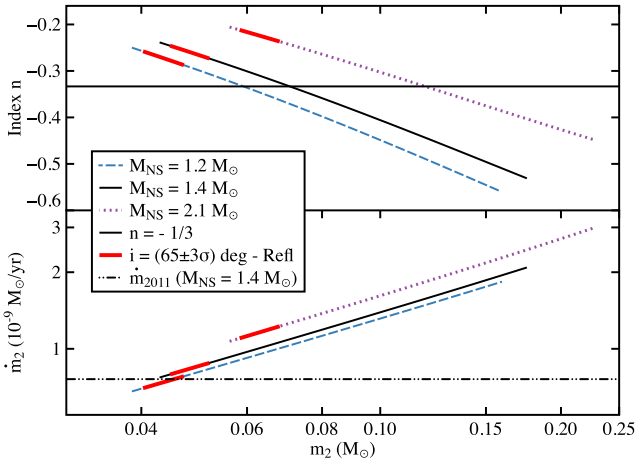

Figure 8. Top panel: mass–radius index versus mass of the companion star evaluated assuming a highly non-conservative ($\beta \sim 0.01$) secular mass transfer scenario for the binary system, with mass ejected at the inner Lagrangian point L_1 (see the text for details on the model). Blue dashed line, black solid line and purple dotted line have been estimated by assuming a NS mass of 1.2, 1.4 and 2.1 $M_\odot$, respectively. The horizontal black line represents the mass–radius index $n = -1/3$ characterizing fully convective stars. Bottom panel: mass-loss rate versus mass of the companion star predicted by adopting the finding reported in the top panel. The horizontal dot-dot–dashed line represents the inferred bolometric mass accretion rate extrapolated from the peak of the 2011 outburst of the source. Mass values of the companion star mass have been estimated from the binary mass function assuming inclination angles between 90° and 15°(corresponding to the 95 per cent confidence level; see e.g. Chakrabarty & Morgan 1998). Red-solid segments highlight the values of n and $\dot{m}_2$ corresponding to the orbital inclination ($i = 65° \pm 9°$) derived from the modelling of the reflection spectrum observed during the latest outburst of the source.

represents the mass–radius index $n = -1/3$, typically used to describe degenerate or fully convective stars. Taking into account the binary inclination ($i = 65° \pm 9°$ with a 3σ confidence level uncertainty) derived from the spectral properties of the reflection spectrum modelled from the *XMM–Newton* and *NuSTAR* observation of the latest outburst (Di Salvo et al., in preparation), we predict the mass and the mass–radius index of the companion mass (red solid lines in Fig. 8) to be $m_2 = (0.04–0.047)$ $M_\odot$ and $n = -(0.29 - 0.27)$, $m_2 = (0.044–0.052)$ $M_\odot$ and $n = -(0.27 - 0.26)$ and $m_2 = (0.062–0.068)$ $M_\odot$ and $n = -(0.24 - 0.22)$ for a NS mass of 1.2, 1.4 and 2.1 $M_\odot$, respectively. It is worth noting that, even though the companion mass values are well below 0.1 $M_\odot$, the mass–radius index appears slightly larger than $n = -1/3$, predicted for star that became fully convective (see e.g. King 1988; Verbunt 1993). This discrepancy could reflect the different secular evolution that the companion star may experience within the binary system compared to a standard isolated star. Nonetheless, the effect of the direct X-ray and magnetic dipole irradiation of the companion star during the outburst activity and the quiescence phase, respectively, could likely modify the mass–radius hydrostatic equilibrium relation of the star. Bottom panel of Fig. 8 shows the predicted companion star mass transfer rate estimated by substituting m_1, m_2 and n reported in the top panel of Fig. 8. As a reference, we show the mass accretion rate measured during the peak of the 2011 X-ray outburst of the source, inferred assuming a source distance of 3.5 kpc. In line with Di Salvo et al. (2008) and Burderi et al. (2009), we suggest that the up-to-date measured value of the orbital period derivative (reflecting a long-term evolution of 17 yr) is compatible with a highly non-conservative mass transfer scenario where almost 99 per cent of the matter transferred from the companion star is ejected from the system and not directly observed.

4.3.4 Radio-ejection mechanism

The proposed mechanism to expel the accreting matter from the system involves radiation pressure of the magneto-dipole rotator that should power the NS during quiescence phases (see e.g. Burderi et al. 2003; Di Salvo et al. 2008). Over the years several indirect hints that in SAX J1808.4−3658 the radio pulsar mechanism turns on during quiescence phases have been collected: e.g. the presence of an overluminous optical counterpart of the source (Homer et al. 2001) interpreted by Burderi et al. (2003) as the spin-down luminosity of the magneto-dipole rotator reprocessed by the companion star; the secular spin-down evolution of the NS spin showing derivative values typical of millisecond radio pulsars (Hartman et al. 2009b; Patruno et al. 2012); detection of a possible gamma-ray counterpart of the source as observed by *Fermi*-Large Area Telescope (LAT) during the quiescence phases of SAX J1808.4−3658 (Xing, Wang & Jithesh 2015; de Oña Wilhelmi et al. 2016). Nonetheless, although carefully searched (Burgay et al. 2003; Patruno et al. 2017), no direct observation of the radio pulsar activity of the source has been observed to date (at this moment the only known AMXP observed as rotation-powered pulsar is IGR J18245−2453; Papitto et al. 2013). In analogy with the black widows in the stage of the so-called star-vapourizing pulsars or hidden millisecond pulsars (e.g. Tavani 1991), Di Salvo et al. (2008) suggested that the radio emission from the rotation-powered pulsar is completely blocked by material engulfing the system likely generated from the interaction between the pulsar radiation pressure and the mass overflowing from the companion star (the so-called hidden black widow scenario). X-ray outbursts would then be triggered by temporary increase of pressure of the overflowing matter sufficient to overcome the radiation pressure of the rotation-powered pulsar. Discrepancies observed around the almost constant secular expansion of the orbital period (Fig. 7, bottom left-hand panel) could then reflect stochastic fluctuations of the radiation pressure regulating the mass-loss rate, or of the mass transfer rate itself.

Hartman et al. (2009b) verified the energetic feasibility of the aforementioned scenario showing that the spin-down luminosity of SAX J1808.4−3658 in quiescence (estimated from the observed long-term spin-down of the pulsar) could drive a mass loss from the companion of the order of 10^{-9} $M_\odot$ yr^{-1}, compatible with our findings reported above. However, the authors raised doubts on the possibility to preserve the accretion disc during the activity of the particle wind, hence the possibility to switch from rotation-powered to accretion-powered pulsar.

5 CONCLUSIONS

In this paper, we presented an analysis of the *XMM–Newton* and *NuSTAR* observations collected during the 2015 outburst of SAX J1808.4−3658. From the timing analysis of the two data sets, we determined an updated set of ephemeris of the source. We investigated the time evolution of the spin frequency by means of pulse phase timing techniques applied to the fundamental and the second harmonic components used to describe the coherent signal. We reported significant spin frequency derivative values from the analysis of the fundamental component of both data sets. Moreover, for *XMM–Newton*, we observed a clear mismatch between the time

evolution of the fundamental and its second harmonic component, likely connected to the phase-jumping phenomenon responsible of the strong timing noise present in this source. We extended the study of the secular spin evolution combining the frequency estimates from the previous six outbursts observed between 1998 and 2011 with the value estimated from the analysis of the second harmonic component during the latest outburst in 2015. From the best-fitting linear model, we estimated a long-term spin frequency derivative of $\sim -1.5 \times 10^{-15}$ Hz s^{-1}, compatible with a NS magnetic field of $B \sim 2 \times 10^{8}$ G. Furthermore, we estimated possible corrections to the magnetic field taking into account the effect of mass accretion on to the NS during the outbursts. Combining the seven monitored outbursts of the source, we confirmed the fast orbital expansion of SAX J1808.4−3658 characterized by an average orbital period derivative of $\sim 3.6 \times 10^{-12}$ s s^{-1}, not compatible with a conservative mass transfer scenario driven by GR. We investigated the possibility to explain the observed orbital evolution with the GQC model (Applegate 1992). We found that, for the specific case of SAX J1808.4−3658, such a scenario would require a strong magnetic field (several kG) powered by a tidal dissipation mechanism acting on the companion star. Moreover, this scenario would also imply a large fraction of ejected matter that would strongly influence the orbital evolution of the system. We suggest that under specific conditions this scenario is compatible with the observed orbital evolution of SAX J1808.4−3658. Finally, we also discuss the large and almost stable long-term orbital period derivative characterizing SAX J1808.4−3658 in terms of a highly non-conservative mass transfer scenario, where a large fraction (∼99 per cent) of the mass transferred from the companion star is ejected from the inner Lagrangian point as a consequence of the irradiation from the magneto-dipole rotator during the quiescent phase of the system (*radio-ejection* model). In both cases, therefore, the mass transfer in the system has to be highly not conservative. The main difference is that in the first scenario matter is expelled along the magnetic field lines of the companion with a lever arm of half the orbital separation along the line connecting the two stars with the specific angular momentum with respect to the centre of mass of the system; this is needed in order to power GQC oscillations via tidal dissipation. On the other hand, in the second scenario matter is expelled directly at the inner Lagrangian point, and the variations of the orbital period with respect to the global parabolic trend are caused by random fluctuations of the mass transfer rate. Indeed it is not excluded that the *radio-ejection* mechanism could cause the strong outflow of matter necessary to power the GQC oscillations via tidal dissipation. Future outbursts of the source will be crucial to further investigate between the two main mechanisms described above.

ACKNOWLEDGEMENTS

We gratefully acknowledge the Sardinia Regional Government for the financial support (P. O. R. Sardegna F.S.E. Operational Programme of the Autonomous Region of Sardinia, European Social Fund 2007-2013 – Axis IV Human Resources, Objective l.3, Line of Activity l.3.1). This work was partially supported by the Regione Autonoma della Sardegna through POR-FSE Sardegna 2007–2013, L.R. 7/2007, Progetti di Ricerca di Base e Orientata, Project No. CRP-60529. We also acknowledge financial contribution from the agreement ASI-INAF I/037/12/0. AP acknowledges funding from the European Union's Horizon 2020 research and innovation programme under the Marie Skłodowska-Curie grant agreement 660657-TMSP-H2020-MSCA-IF-2014, and the International Space Science Institute (ISSIBern) that funded and hosted the international team 'The disk magnetosphere interaction around transitional millisecond pulsar'.

REFERENCES

Applegate J. H., 1992, ApJ, 385, 621
Applegate J. H., Shaham J., 1994, ApJ, 436, 312
Archibald A. M., Kaspi V. M., Hessels J. W. T., Stappers B., Janssen G., Lyne A., 2013, ApJ, preprint (arXiv:1311.5161)
Arzoumanian Z., Fruchter A. S., Taylor J. H., 1994, ApJ, 426, 85
Bhattacharya D., van den Heuvel E. P. J., 1991, Phys. Rep., 203, 1
Bildsten L., Chakrabarty D., 2001, ApJ, 557, 292
Burderi L., Di Salvo T., D'Antona F., Robba N. R., Testa V., 2003, A&A, 404, L43
Burderi L., Di Salvo T., Menna M. T., Riggio A., Papitto A., 2006, ApJ, 653, L133
Burderi L. et al., 2007, ApJ, 657, 961
Burderi L., Riggio A., di Salvo T., Papitto A., Menna M. T., D'Aì A., Iaria R., 2009, A&A, 496, L17
Burderi L., Di Salvo T., Riggio A., Papitto A., Iaria R., D'Aì A., Menna M. T., 2010, A&A, 515, A44
Burgay M., Burderi L., Possenti A., D'Amico N., Manchester R. N., Lyne A. G., Camilo F., Campana S., 2003, ApJ, 589, 902
Cackett E. M., Altamirano D., Patruno A., Miller J. M., Reynolds M., Linares M., Wijnands R., 2009, ApJ, 694, L21
Campana S. et al., 2002, ApJ, 575, L15
Campana S. et al., 2004, ApJ, 614, L49
Casella P., Altamirano D., Patruno A., Wijnands R., van der Klis M., 2008, ApJ, 674, L41
Chabrier G., Baraffe I., 1997, A&A, 327, 1039
Chakrabarty D., Morgan E. H., 1998, Nature, 394, 346
Cui W., Morgan E. H., Titarchuk L. G., 1998, ApJ, 504, L27
Deeter J. E., Boynton P. E., Pravdo S. H., 1981, ApJ, 247, 1003
Deloye C. J., Heinke C. O., Taam R. E., Jonker P. G., 2008, MNRAS, 391, 1619
de Oña Wilhelmi E. et al., 2016, MNRAS, 456, 2647
Di Salvo T., Burderi L., 2003, A&A, 397, 723
Di Salvo T., Burderi L., Riggio A., Papitto A., Menna M. T., 2008, MNRAS, 389, 1851
Doroshenko O., Löhmer O., Kramer M., Jessner A., Wielebinski R., Lyne A. G., Lange C., 2001, A&A, 379, 579
Falanga M., Titarchuk L., 2007, ApJ, 661, 1084
Falanga M. et al., 2005, A&A, 444, 15
Friedman B., Pandharipande V. R., 1981, Nucl. Phys. A, 361, 502
Galloway D. K., Cumming A., 2006, ApJ, 652, 559
Galloway D. K., Muno M. P., Hartman J. M., Psaltis D., Chakrabarty D., 2008, ApJS, 179, 360
Goldreich P., Julian W. H., 1969, ApJ, 157, 869
Hameury J.-M., 1996, A&A, 305, 468
Hameury J.-M., Ritter H., 1997, A&AS, 123, 273
Hartman J. M. et al., 2008, ApJ, 675, 1468
Hartman J. M., Watts A. L., Chakrabarty D., 2009a, ApJ, 697, 2102
Hartman J. M., Patruno A., Chakrabarty D., Markwardt C. B., Morgan E. H., van der Klis M., Wijnands R., 2009b, ApJ, 702, 1673
Hirotani K., 2006, ApJ, 652, 1475
Homer L., Charles P. A., Chakrabarty D., van Zyl L., 2001, MNRAS, 325, 1471
Ibragimov A., Poutanen J., 2009, MNRAS, 400, 492
in 't Zand J. J. M., Heise J., Muller J. M., Bazzano A., Cocchi M., Natalucci L., Ubertini P., 1998, A&A, 331, L25
King A. R., 1988, QJRAS, 29, 1
Kirsch M. G. F., Mukerjee K., Breitfellner M. G., Djavidnia S., Freyberg M. J., Kendziorra E., Smith M. J. S., 2004, A&A, 423, L9
Lazaridis K. et al., 2011, MNRAS, 414, 3134
Lyne A. G., Graham-Smith F., 1990, Pulsar Astronomy. Cambridge Univ. Press, Cambridge
Madsen K. K. et al., 2015, ApJS, 220, 8

Meyer F., Meyer-Hofmeister E., 1982, A&A, 106, 34
Muno M. P., Özel F., Chakrabarty D., 2002, ApJ, 581, 550
Muno M. P., Özel F., Chakrabarty D., 2003, ApJ, 595, 1066
Paczyński B., 1971, ARA&A, 9, 183
Pandharipande V. R., Ravenhall D. G., 1989, in Soyeur M., Flocard H., Tamain B., Porneuf M., eds, NATO Advanced Science Institutes (ASI) Series B, Vol. 205, Nuclear Matter and Heavy Ion Collisions. Plenum Press, New York, p. 103
Papitto A., Di Salvo T., D'Aì A., Iaria R., Burderi L., Riggio A., Menna M. T., Robba N. R., 2009, A&A, 493, L39
Papitto A., Riggio A., di Salvo T., Burderi L., D'Aì A., Iaria R., Bozzo E., Menna M. T., 2010, MNRAS, 407, 2575
Papitto A. et al., 2013, Nature, 501, 517
Patruno A., Rea N., Altamirano D., Linares M., Wijnands R., van der Klis M., 2009a, MNRAS, 396, L51
Patruno A., Altamirano D., Hessels J. W. T., Casella P., Wijnands R., van der Klis M., 2009b, ApJ, 690, 1856
Patruno A., Wijnands R., van der Klis M., 2009c, ApJ, 698, L60
Patruno A., Altamirano D., Messenger C., 2010, MNRAS, 403, 1426
Patruno A., Bult P., Gopakumar A., Hartman J. M., Wijnands R., van der Klis M., Chakrabarty D., 2012, ApJ, 746, L27
Patruno A. et al., 2017, ApJ, 841, 98
Pintore F. et al., 2014, MNRAS, 445, 3745
Pletsch H. J., Clark C. J., 2015, ApJ, 807, 18
Podsiadlowski P., 1991, Nature, 350, 136
Poutanen J., Gierliński M., 2003, MNRAS, 343, 1301
Pringle J. E., Rees M. J., 1972, A&A, 21, 1
Reiners A., 2012, Living Rev. Sol. Phys., 9, 1
Riggio A., Papitto A., Burderi L., di Salvo T., 2011, in Burgay M., D'Amico N., Esposito P., Pellizzoni A., Possenti A., eds, AIP Conf. Proc. Vol. 1357, Radio Pulsars: An Astrophysical Key to Unlock the Secrets of the Universe. Am. Inst. Phys., New York, p. 151
Roche P., Chakrabarty D., Morales-Rueda L., Hynes R., Slivan S. M., Simpson C., Hewett P., 1998, IAU Circular, 6885, 1
Sanna A. et al., 2015, Astron. Telegram, 7371, 1
Sanna A. et al., 2016, MNRAS, 459, 1340
Sanna A. et al., 2017, MNRAS, 466, 2910
Shaifullah G. et al., 2016, MNRAS, 462, 1029
Smak J., 1982, Acta Astron., 32, 199
Spitkovsky A., 2006, ApJ, 648, L51
Stenson E. V., Horn-Stanja J., Stoneking M. R., Pedersen T. S., 2017, J. Plasma Phys., 83
Tailo M. et al., 2015, Nature, 523, 318
Tailo M., Di Criscienzo M., D'Antona F., Caloi V., Ventura P., 2016, MNRAS, 457, 4525
Tavani M., 1991, ApJ, 379, L69
Ventura P., Zeppieri A., Mazzitelli I., D'Antona F., 1998, A&A, 334, 953
Ventura P., D'Antona F., Mazzitelli I., 2008, Ap&SS, 316, 93
Verbunt F., 1993, ARA&A, 31, 93
Wijnands R., van der Klis M., 1998, Nature, 394, 344
Wolff M. T., Ray P. S., Wood K. S., Hertz P. L., 2009, ApJS, 183, 156
Xing Y., Wang Z., Jithesh V., 2015, PASJ, preprint (arXiv:1502.00733)

This paper has been typeset from a TEX/LATEX file prepared by the author.